Materials Today Bio 30 (2025) 101448

Contents lists available at ScienceDirect

Materials Today Bio

journal homepage: www.journals.elsevier.com/materials-today-bio

Matrix vesicle-inspired delivery system based on nanofibrous chitosan microspheres for enhanced bone regeneration

Haolin Bian [a,b,1], Fangfang Song [a,1], Shilei Wang [c], Wei Sun [a], Bo Hu [d], Xichao Liang [d], Hongye Yang [a,**], Cui Huang [a,*]

[a] State Key Laboratory of Oral & Maxillofacial Reconstruction and Regeneration, Key Laboratory of Oral Biomedicine Ministry of Education, Hubei Key Laboratory of Stomatology, School & Hospital of Stomatology, Wuhan University, Wuhan, 430079, China
[b] Department of Stomatology, The First Affiliated Hospital, College of Medicine, Zhejiang University, Hangzhou, 310003, China
[c] Key Laboratory of Resources and Compound of Traditional Chinese Medicine, Ministry of Education, Hubei University of Traditional Chinese Medicine, Wuhan, 430065, China
[d] Research and Application of Regenerative Cellulose Fiber Key Laboratory of Sichuan Province, YiBin Grace Group Co., LTD, Yibin, 644000, China

ARTICLE INFO

Keywords:
Nanofibrous chitosan microsphere
Matrix vesicles
Amorphous calcium phosphate
Collagen mineralization
Osteogenesis
Tissue engineering

ABSTRACT

Inspired by the initial mineralization process with bone matrix vesicles (MVs), this study innovatively developed a delivery system to mediate mineralization during bone regeneration. The system comprises nanofibrous chitosan microspheres (NCM) and poly (allylamine hydrochloride)-stabilized amorphous calcium phosphate (PAH-ACP), which is thereafter referred to as NCMP. NCM is synthesized through the thermal induction of chitosan molecular chains, serving as the carrier, while PAH-ACP functions as the mineralization precursor. Additionally, the nanofibrous network of NCMP mimics the architecture of natural extracellular matrix (ECM), creating an optimal niche for the active adhesion of stem cells to its surface, exhibiting good biocompatibility, immunoregulation, and osteogenic performance. *In vivo*, NCMP effectively recruits cells and mineralizes collagen, modulates cell behavior and differentiation, and promotes *in situ* biomineralization in rat calvarial defects. These results underscore the dual efficacy of NCMP not only as an effective delivery system for mineralization precursors but also as ECM-mimicking bio-blocks, offering a promising avenue for enhancing the repair and regeneration of bone defects.

1. Introduction

Bone is a specialized form of connective tissue mainly composed of an inorganic mineral matrix and an organic collagen network, the combination of which confer bone the ideal properties of strength and rigidity [1]. The complete regeneration of large-scale bone defects resulting from traumatic fracture, osteoporosis, abnormalities, or bone tumors, remains a significant challenge [2]. At present, autografts are considered as the gold standard for treating critical-sized bone defects [3]. However, the limited availability of autograft sources severely restricts their application [4], not to mention the potential for complications from additional surgeries [5]. Bone tissue engineering (BTE) is transforming the bone-grafting materials to treating bone defect and has the potential to significantly improve the quality of life for millions of individuals [6]. Currently, most biomaterials emulate various compositions of inorganic substances, such as hydroxyapatite (HAp), bioactive glasses, and calcium phosphates, along with organic matrix, like collagen [7]. Simply combination of inorganic and organic components cannot accurately replicate the complexity and phases of mineralization [8]. Bone repairing is a highly dynamic process, involving the regulation of biological signals and the orderly crystallization of inorganic components, known as biomineralization [9].

Abbreviations: ECM, Extracellular matrix; NCM, Nanofibrous chitosan microsphere; MVs, Matrix vesicles; ACP, Amorphous calcium phosphate; HAp, Hydroxyapatite; BMSCs, Bone marrow stromal cells; PILP, Polymer-induced liquid-precursor; PAsp, Polyaspartic acid; PAA, Polyacrylic acid; PAH, Poly(allylamine hydrochloride); PAMAM, Poly(amidoamine)..

* Corresponding author.
** Corresponding author.
E-mail addresses: yanghongye@whu.edu.cn (H. Yang), huangcui@whu.edu.cn (C. Huang).
[1] Haolin Bian and Fangfang Song contributed equally to this study.

https://doi.org/10.1016/j.mtbio.2025.101448
Received 16 October 2024; Received in revised form 1 January 2025; Accepted 3 January 2025
Available online 3 January 2025

Biomineralization processes in vertebrates inspire the fabrication of smart organic-inorganic hybrid biomaterials, with the primary objective of BTE being to enhance biomineralization in defect regions and create nano-, micro-, and macro-level structures of bone for repair and regeneration [3,10].

In biomineralization, amorphous calcium phosphate (ACP) is the initial mineral phase formed and is widely utilized in biomimetic mineralization efforts. Calcium and phosphate are transported and accumulated within matrix vesicles (MVs) to form amorphous ACP, which then undergoes a transformation into hydroxyapatite, effectively initiating the mineralization process [11]. This process has been engineered and mimicked for use in bone tissue engineering applications [12]. MVs are spherical and electron-dense microparticles ranging from 100 to 300 nm in diameter [13,14], which are unique extracellular membrane-bound microparticles that serve as initial sites for mineralization [14,15]. These vesicles are believed to play a critical role in various forms of physiological or ectopic calcification, including those occurring in bone and teeth [16–18]. Previous study has developed bioinspired MVs embedded with black phosphorus (BP) for stimulating biomineralization [19], which display outstanding bone regeneration performance. Inspired by the role of MVs in biomineralization, we aim to design bioinspired bone grafting materials that mimic the function of MVs by supplying sufficient stabilized ACP precursors for the biomineralization process.

Collagen biomineralization involves both intrafibrillar mineralization and extrafibrillar mineralization [20,21], reflecting the spatial distribution of apatite between and within collagen fibrils through the infiltration of stabilized ACP [22–25]. As the first-formed mineral phase in biomineralization, ACP is widely used in biomimetic mineralization. Additionally, ACP can provide a chemical environment enriched with calcium and phosphate, which stimulates osteogenic differentiation of stem cells [26,27]. However, due to their thermodynamic instability and rapid phase-transition properties, supersaturated ACP solutions often undergo premature crystallization, which hinders their effectiveness in biomineralization [28,29]. To solve this problem, scientists have demonstrated the effectiveness of polymer-induced liquid-precursor (PILP) in mediating intrafibrillar mineralization, which is defined as an amorphous liquid-phase mineral precursor sequestered by biomimetic molecules as substitutes for non-collagenous proteins, such as polyaspartic acid (PAsp), polyacrylic acid (PAA), poly(allylamine hydrochloride) (PAH) and poly(amidoamine) (PAMAM) [25,30–32]. The PAH-stabilized ACP has been recently proven to penetrate the gap zone of collagen fibrils and then transform into oriented apatite crystals, achieving intrafibrillar mineralization of collagen [25]. Since the PILP phases of ACP are prepared via liquid–liquid phase separation from supersaturated calcium and phosphate-containing solutions, it is challenging to retain them in sufficient quantities within a surgical site when dispersed in solution [33]. Therefore, designing a delivery system for PAH-stabilized ACP is essential for effectively storing and transporting it to the bone defect site.

Chitosan, a derivative of chitin produced through N-deacetylation, is a linear polysaccharide composed of D-glucosamine (GlcN) and N-acetyl-d-glucosamine (GlcNAc) [34]. Its structure and composition are similar to the major components of the extracellular matrix (ECM) glycosaminoglycans [35]. Chitosan is a natural basic amino polysaccharide, known for its positive charge and remarkable properties such as biodegradability, biocompatibility, bioactivity, and low immunogenicity [36]. These attributes make chitosan ideal for use in tissue engineering with ECM-mimicking nanofibrous structures. In our previous work, we successfully developed nanofibrous chitosan microspheres (NCM) using an alkaline/urea aqueous solvent method for cell delivery [37]. These microparticles feature an interconnected nanofibrous structure mimicking the three-dimensional (3D) microenvironment of the ECM, thereby supporting cell growth and infiltration [38]. Thus, these properties enable NCM to serve as an ideal carrier for ACP precursors.

Inspired by the role of MVs in the biomineralization process, this study developed a biomimetic delivery system by constructing NCM loaded with PAH-stabilized ACP mineral precursors (NCMP), which not only provides the ECM-mimicking structure to direct cell growth, but also releases sufficient stabilized ACPs that specifically guides collagen mineralization. Leveraging this bioinspired design, our strategy proposes a potential strategy for creating biofunctional materials that regulate biological functions and advance the field of biomedical engineering.

2. Materials and methods

2.1. Chemicals and agents

Unless otherwise noted, chemicals and reagents of analytical grade were purchased from Sigma-Aldrich, Inc. (Missouri, USA). All chemicals and reagents were used without further purification.

2.2. Synthesis of nanofibrous chitosan microspheres (NCM), HAp@NCM (NCMH) and PAH-ACP@NCM (NCMP)

Nanofibrous chitosan microspheres (NCM) were synthesized following our established protocols using a sol-gel transition process [37]. First, 4.5 g of chitosan powder was mixed with 95.5 g of an alkaline aqueous solvent (LiOH, KOH, urea, and deionized water in a 4.5:7:8:80.5 wt ratio) to form a suspension. This solution was frozen at −40 °C for 4 h and then thawed at room temperature, followed by two additional freezing-thawing cycles to obtain a transparent chitosan solution (4.5 wt%). The chitosan solution was then combined with isooctane and Span 80, stirred in an ice bath, and subsequently heated in a 60 °C water bath for 30 min to induce sol-gel transition. Finally, the resulting solution was transferred to ethanol/water, and NCM were prepared for the following experiments.

PAH powders were dissolved into 9 mM $CaCl_2{\cdot}2H_2O$ at room temperature at a concentration of 1000 μg/mL. An equal volume of 4.2 mM $Na_2HPO_4{\cdot}12H_2O$ was then added to this solution to prepare the PAH-ACP solution (Final concentrations: Ca^{2+}at 4.5 mM, HPO_4^{2-}at 2.1 mM, and PAH at 500 μg/mL in Tris-buffered saline (TBS) solution). To prepare PAH-ACP@NCM (NCMP), 400 mg of NCM was dispersed in 100 mL of the PAH-ACP solution and mixed for 24 h at 25 °C to achieve equilibrium. For comparison, Hydroxyapatite-loaded NCM (HAp@NCM, referred to as NCMH) were also prepared by dispersing NCM into a Ca/P solution (Final concentrations: Ca^{2+}at 4.5 mM and HPO_4^{2-}at 2.1 mM in TBS solution). The resulting white precipitate was then heated at 80 °C for 48 h to accelerate crystal formation, thereby transforming into HAp. After centrifuge, NCMP and NCMH were washed with TBS two times, vacuum freeze-dried, and then preserved at −20 °C until use.

2.3. Characterization of microspheres

2.3.1. SEM, EDX, FTIR and XRD

The surface morphology and element distribution of NCM, NCMH and NCMP were examined using field-emission scanning electron microscopy (FE-SEM, Zeiss SIGMA, Britain). Each sample was vacuum freeze-dried and coated with gold. Elemental mapping was conducted using Oxford UltimMax 40 (FEI, Hillsboro, OR) at 20 kV. The size distributions of NCMP were assessed via ImageJ (NIH, Frederick, MD, USA) with captured SEM images. Fourier Transform infrared spectroscopy (FT-IR) was applied to analyze the physical or chemical interactions between different components. Each spectrum was recorded using the

KBr pellet method on an FT-IR spectrophotometer (model 1600, Perkin-Elmer Co., USA) spanning 4000 to 400 cm^{-1}. Wide-angle X-Ray Diffraction (XRD) was carried out on an X-ray diffractometer (SmartLab 9 kW, Rigaku, Japan) with Cu−Kα radiation at 40 kV and 40 mA, and the results were collected from 2θ = 3–60° at a scan rate of 2°/min. Three independent samples were measured for each experiment.

2.3.2. Release of Calcium (Ca) and Phosphate (P)

200 mg of NCMP was placed in a centrifugal tube with 10 mL of deionized water and incubated on a shaker at 37 °C. At predetermined time points (0, 0.5, 1, 2, 4, 6, 16, 24, 48, 72, 120 and 148 h), 1 mL of supernatant was collected and replaced with an equal volume of deionized water for ions detection. The liquid samples were analyzed using inductively coupled plasma–atomic emission spectroscopy (ICP-AES) (IRIS Intrepid II XSP, Thermo Fisher Scientific Inc., Waltham, MA, USA) to quantify the Ca and P content.

2.3.3. Zeta (ζ) potentials

The zeta potential of samples (NCM, NCMP and PAH-ACP) was analyzed with the Zetasizer Nano ZS system (Malvern Instruments Ltd., Westborough, MA, USA) (n = 4). The materials were dispersed in pure water (pH = 7.0) and the zeta potential measurements were taken immediately following 15 min of ultrasonication.

2.3.4. Atomic force microscopy

The surface morphological characteristics of NCM, NCMH, and NCMP were characterized using atomic force microscopy (AFM, Multi-Mode 8, Bruker, Santa Barbara, CA, USA). The samples of different groups were dispersed on the conductive adhesives affixed to a metallic substrate and then scanned using a diamond probe in tapping mode (n = 3).

2.3.5. Mechanical test

The mechanical property of microspheres was measured using a universal testing machine (CMT 6503, SANS). During the test, microspheres gently filled up the chamber of a hollow cylinder with diameter of 3.5 mm and height of 10 mm, then the compressive stress was evaluated according to ISO527-3-1995 (E) at a speed of 2 mm/min (n = 3).

2.4. Collagen intrafibrillar mineralization

Single-layer collagen models were prepared for intrafibrillar mineralization. Type I collagen powder, derived from rat tail tendon, was dissolved in sterilized 17.5 mM acetic acid at a concentration of 0.2 mg/mL for collagen assembly. Nickel TEM grids with 200-mesh (XXBR Technology, Beijing, China) were placed onto the collagen solution. The pH of the collagen solution was adjusted to 8 with ammonia vapor. After removing excess solution and air-drying, self-assembled collagen fibrils were deposited on the TEM grids.

50 mg of different microspheres were immersed in 1 mL of Simulated Body Fluid (SBF, MesGen Biotech, Shanghai, China) in each well of a 12-well plate (n = 3). TEM grids covered with reconstituted collagen fibrils were plated on the surface of the suspension. The assembly was incubated in a 100 % relative humidity chamber at 37 °C. Grids were collected after 1, 3, or 5 days for TEM observation (JEM-2100, JEOL, Japan). Crystallinity was assessed through selected area electron diffraction (SAED).

2.5. Biocompatibility assessment

2.5.1. Cell morphology and proliferation

Human dental pulp stem cells (hDPSCs) were isolated from fresh third molars of healthy adults aged 18–26 years old [39], following informed consent and in accordance with a protocol approved by the Ethics Committee of the Hospital of Stomatology, Wuhan University. Cells were cultured in complete medium consisting of α-MEM (Gibco, USA) supplemented with 10 % fetal bovine serum (FBS, Gibco, USA), 100 U/mL penicillin, and 100 μg/mL streptomycin. Cells were monitored under a microscope until they reached 90 % confluency, at which point they were passaged using enzymatic digestion. Prior to the synthesis of NCMP, the raw materials were sterilized by autoclaving. Cell Count Kit-8 (CCK-8, Dojindo, Japan) assay was used to determine cell proliferation. Suspension of cells and NCMP in complete medium were seeded in 96-well plates and incubated at 37 °C for specific intervals of 1, 3, 5, and 7 days (n = 9). After removing the medium, and 10 % CCK-8 solution was added to each well. Following a 2-h incubation, the absorbance were determined at 450 nm. Crystal violet (CV) staining was applied for cell proliferation images. Cells were washed with Phosphate Buffered Saline (PBS), fixed with 4 % Paraformaldehyde, and stained with 1 mL CV stain. Coomassie bright blue (CBB) staining was performed for assessing cell morphology. Cells were permeabilized with 0.1 % Triton for 15 min at 37 °C, fixed with 4 % Paraformaldehyde and washed with PBS, followed by staining with CBB solution. The cell morphology and proliferation images were captured with an Inverted Microscope. The control group indicates that no NCMP were added. All the experiments were performed in triplicate. Three independent experiments have been performed.

2.5.2. Hemolysis tests

Fresh blood was obtained from 8-week-old Sprague-Dawley (SD) rats and diluted with PBS in a 4:5 vol ratio. NCMP was immersed in PBS at a concentration of 1 mg/mL and kept at 37 °C for 60 min. PBS and ddH_2O were used as negative controls (C-) and positive controls (C+), accordingly. Diluted blood was then added to each setup in a 1:5 vol ratio, and the mixtures were incubated at 37 °C for 1 h. After centrifugation at 1690*g* for 5mins, the supernatant was collected and its absorption at 545 nm was determined. All experiments were performed in triplicate. Three independent experiments have been performed. The hemolysis rate (HR) was calculated using the following equation:

$$\mathrm{HR}(\%) = \frac{OD_{NCMP} - OD_{C-}}{OD_{C+} - OD_{C-}} \times 100\ \% \quad (1)$$

2.5.3. In vitro/vivo degradation

To determine the *in vitro* swelling behavior and degradation properties of NCMP, 10 mg NCMP dry powder (set as W_0) was added to the upper chambers of a 12-well transwell plate (n = 5), fully immersed either in pure Tris Buffered Saline (TBS, pH = 7.4) or a lysozyme solution (Macklin Biochemical Co. Shanghai, China) at concentrations of 1 and 10 mg/mL dissolved in TBS solution at 37 °C. After 12 h, the wet gross weight (defined as W_1) was recorded after removing any surface liquid. The buffer solution was replaced every two days to maintain enzyme activity. At specified time points (12 h, 1, 2, 3, 5, 7, 9, 12, 15, 18 and 21 days), the upper chamber was removed, and the gross wet weight (defined as W_2) was measured after removal of any remaining fluid by filter paper. The fluid absorption rate (AR, at 12 h) and degradation rate (DR) were calculated using the following formula. All the experiments were performed in triplicate. Three independent experiments have been performed.

$$\mathrm{AR}\ (\%) = \frac{W_1 - W_0}{W} \times 100\ \% \quad (2)$$

$$\mathrm{DR}\ (\%) = \frac{W_2 - W_1}{W} \times 100\ \% \quad (3)$$

All animal experiments were conducted in accordance with the ethical policies established by the Ethics Committee for Animal Research at Wuhan University, China (Approval ID: S07920090A). In the *in vivo* degradation experiment, 20 mg sterilized NCMP microspheres were dissolved in saline and then injected subcutaneously into the dorsum of 8-week-old SD rats using syringes. After specific time intervals, the samples were harvested and fixed in 4 % polyformaldehyde overnight, followed by two consecutive overnight immersions in PBS. The samples were then embedded in paraffin, sectioned at a thickness of 5 μm, and subjected to HE staining. Three stained sections from independent experiments were imaged using a Pannoramic MIDI Slide scanner (3D HISTECH).

2.6. Cell adhesion assessment

2.6.1. Cell adhesion

5×10^6 hDPSC cells were combined with 100 mg NCMP in complete medium and seeded into 24-well plates for 7–14 days. The obtained wet gross complex was dried at 37 °C for 6–12 h, washed with PBS, and fixed with 4 % paraformaldehyde. Cell adhesion on the microspheres were observed using inverted microscopes, and detailed observation of cell adhesion and other behaviors were examined using SEM. After being cultured for 1 day and 5 days, the cell-NCMP complex was fixed in 2.5 % glutaraldehyde and washed with PBS. The samples were then dehydrated through a graded ethanol series (55 %, 65 %, 75 %, 85 %, 95 % and 100 %), vacuum freeze-dried, gold coated, and observed with SEM (Ultra 55, ZEISS). All the experiments were performed in triplicate. Three independent experiments have been performed.

2.6.2. Adhesion-related genes expression

The expression levels of specific gene markers related to cell adhesion were studied using real-time quantitative polymerase chain reaction (RT-qPCR). Cell-NCMP (10 mg/mL) suspensions in complete medium were seeded and cultured in 6-well plates (10^6/well) for 1 day (n = 4 independent samples per group). The total RNA was isolated using the Ultrapure RNA Kit (CoWin Biosciences) following the manufacturer's instructions. The concentration and purity of the extracted RNA were assessed using a Nanodrop 2000 spectrophotometer (Thermo Scientific, USA), which measures absorbance at 260 nm and 280 nm. One μg of RNA from each sample was reverse transcribed into complementary DNA (cDNA) with the PrimeScript™ RT reagent Kit with gDNA Eraser (Takara, Japan). The expression levels of specific gene markers, including integrin α5 (ITGA5), integrin α7 (ITGA7), integrin α10 (ITGA10), integrin β5 (ITGB5) and fibronectin 1 (FN1), were quantified using TB Green® Premix Ex Taq™ II (TaKaRa, Japan) on Bio-Rad CFX96. The relative mRNA expression level was normalized to the housekeeping gene glyceraldehyde-3-phosphate dehydrogenase (GAPDH) and determined using cycle threshold (Ct) values (with pure cells as Blank Control). The forward and reverse primers of specific gene markers are listed in Table 1.

Table 1
The qPCR Primer Sequences of Adhesion-Related Genes.

Gene	Primer	Sequences (5′-3′)
GAPDH	Forward	TGTTCGACAGTCAGCCGCAT
	Reverse	CGCCCAATACGACCAAATCCGT
ITGA5	Forward	GTCGGGGGCTTCAACTTAGAC
	Reverse	CCTGGCTGGCTGGTATTAGC
ITGA7	Forward	GGAAGACCGACAGCAGTTCA
	Reverse	ATCTTGATGCGACACCAGCA
ITGA10	Forward	GTGTGGATGCTTCATTCCAG
	Reverse	GCCATCCAAGACAATGACAA
ITGB5	Forward	GGGAGTTTGCAAAGTTTCAGAG
	Reverse	TGTGCGTGGAGATAGGCTTT
FN1	Forward	CTGGCCGAAAATACATTGTAAA
	Reverse	CCACAGTCGGGTCAGGAG

2.6.3. Cytoskeleton staining

The microspheres adhered with hDPSCs were washed with PBS after 1 day or 5 days of culture. The cells were fixed with 4 % Paraformaldehyde and washed with PBS, followed by permeabilization with 0.1 % Triton for 5 min at 25 °C in the dark. Each sample was stained with actin-FITC (fluorescein isothiocyanate) green (Yuanye Bio-Technology, Shanghai, China) for 5 min and with DAPI for 30 s, both at room temperature and protected from light. The cytoskeletal actin and cell nuclei were observed with Confocal Laser Scanning Microscope (Leica-LCS-SP8-STED, Leica, Germany) (n = 3 independent samples per group).

2.7. In vitro osteogenic differentiation

The osteogenic induction medium (OI) was prepared by supplementing the complete medium with 10 mM β-glycerophosphate (β-GP), 100 nM dexamethasone and 50 μg/mL ascorbic acid. The OI medium was refreshed every 2 days during the osteogenic differentiation of hDPSCs.

2.7.1. Alkaline phosphatase activity and Alizarin Red Staining

Cell-microsphere (10 mg/mL) suspension in OI medium was seeded into 12-well plates and cultured for 7–21 days for the respective experiments. For Alkaline phosphatase (ALP) and Alizarin Red Staining (ARS) staining, samples were washed with PBS, fixed in 4 % glutaraldehyde, and stained using BCIP/NBT Alkaline Phosphatase Color Development Kit (PH = 9.8, Beyotime, Shanghai, China) or ARS solution (Servicebio, pH = 8.3) for 2 h. The wells were then rinsed with distilled water to remove the nonspecific staining. All the staining results were observed and captured with inverted microscopes. For quantitative analysis of ARS, the stained samples were incubated with 10 % cetylpyridinium chloride solution (dissolved in 10 mM Na_3PO_4), and absorbance at 620 nm was recorded and analyzed.

For ALP activity, each sample was lysed with 1 % Triton X-100 and centrifuged at 12000 rpm (13523g) for 10 min. The supernatant was then incubated with the Alkaline Phosphatase Assay Kit (Beyotime, Shanghai, China), and the absorbance at 405 nm was measured. The ALP activity of each group was finally normalized to the total proteins using the bicinchoninic acid (BCA) Protein Assay Kit (Biosharp, Hefei, Anhui, China).

2.7.2. Osteogenesis-related genes expression

The expression levels of specific gene markers of osteogenic differentiation were investigated by RT-qPCR. Cell-microsphere (10 mg/mL) suspensions were seeded in 6-well plates and cultured in OI medium for either 1 or 2 weeks. The isolation of RNA and subsequent reverse transcription into cDNA were performed as previously described (see section 2.6.2). The expression levels of these specific gene markers, including ALP, runt-related transcription factor 2 (RUNX2), osterix (OSX/SP7), osteocalcin (OCN/BGLAP), dentin matrix acidic phosphoprotein 1

Table 2
The qPCR Primer Sequences of Osteogenesis-Related Genes.

Gene	Primer	Sequences (5′-3′)
GAPDH	Forward	TGTTCGACAGTCAGCCGCAT
	Reverse	CGCCCAATACGACCAAATCCGT
ALP	Forward	TAAGGACATCGCCTACCAGCTC
	Reverse	TCTTCCAGGTGTCAACGAGGT
RUNX2	Forward	ACCACAAGTGCGGTGCAAAC
	Reverse	ACTGCTTGCAGCCTTAAATGACTCT
SP7	Forward	AACAGGAGTGGAGCTGGCCT
	Reverse	GCCATAGTGAACTTCCTCCTGGG
BGLAP	Forward	CACCATGAGAGCCCTCACACTC
	Reverse	CCTGCTTGGACACAAAGGCTGC
DMP1	Forward	CAAAGAAGATAGCAACTCCACG
	Reverse	CATCAACTGTTAATTTCCGGCT
DSPP	Forward	GCTGGAAGCAATAACAGTACAG
	Reverse	TGCTGTTGATCTGAGGTGTTAT

Table 3
Primer sequences for qPCR in RAW 264.7.

Gene	Forward 5′-3′	Reverse 5′-3′
Gapdh	CTCGTCCCGTAGACAAAATGGT	GAGGTCAATGAAGGGGTCGTT
Mrc1	AGACGAAATCCCTGCTACTG	CACCCATTCGAAGGCATTC
Il10	AGGCGCTGTCATCGATTTCT	TGGAGTCCAGCAGACTCAAT
Arg1	TACAAGACAGGGCTCCTTTCAG	TGAGTTCCGAAGCAAGCCAA
Itgax	ACTTCACGGCCTCTCTTCC	CACCAGGGTCTTCAAGTCTG
Tnfrsf11a	GCAGCTCAACAAGGATACGG	GGTGCAGTTGGTCCAAGGTT
Mmp9	GGGCGTGTCTGGAGATTCG	CACCTGGTTCACCTCATGGTC

(DMP1) and dentin sialophosphoprotein (DSPP), were normalized to GAPDH for quantitative assessment (n = 4 independent samples per group). The forward and reverse primers of the selected genes are listed in Table 2.

2.8. Macrophage polarization-related genes expression

Mouse macrophages RAW 264.7 were seeded with different microspheres at a density of 10^5/mL and cultured in DMEM (Gibco, USA). To assess the immunomodulatory effects, the cells were co-cultured for 1 and 2 days, followed by analysis of several gene markers via qPCR, involving M1/M2 polarization markers (CD-11c and CD206), anti-inflammatory cytokines (IL-10 and Arg1), and osteoclast-related factors (RANK and MMP9) (n = 3 independent samples per group). The forward and reverse primers of the selected genes are listed in Table 3.

2.9. In vivo bone regeneration

Male 8-week-old SD rats were anesthetized via intraperitoneal injection of 2 % pentobarbital sodium (0.2 mL per 100 g of body weight). All animal experiments were conducted in accordance with the ethical policies set forth by the Ethics Committee for Animal Research at Wuhan University, China (Approval ID: S07920090A).

2.9.1. Bone defect model

The rats were randomly divided into four groups: Blank Control, NCM, NCMH, and NCMP, with 6 animals per group for each time point assessed. A longitudinal incision approximately 2 cm in length was made along the sagittal axis of the skull following thorough disinfection. This incision extended through the full thickness of the skin and periosteum to expose the bone surface. Using a circular drill, two circular defects, each measuring 5 mm in diameter and approximately 1 mm in thickness, were created in the calvarial bone. Two milligrams of dry microspheres from different groups were then implanted and filled up the defect areas according to the designated experimental groups, while the bone defects that received no microspheres were designated as the blank control group. The soft tissues and skin were carefully sutured, and all rats received an intramuscular injection of 0.4 mL penicillin (10^5 IU/mL) for three consecutive days.

2.9.2. Micro-CT evaluation

After implantation for 4 and 8 weeks, the rats were sacrificed, and the newly formed bones at the surgical sites were evaluated using Micro-CT (Skyscan 1276, Brook, Belgium). Each bone sample was fixed in 4 % polyformaldehyde overnight and then immersed in PBS twice for 24 h each. The scanning parameters, including scanning resolution (4.8 μm), rotation angle (180°) and scanning voltage (80 kV), were set consistent across all groups. The bundled software transformed the raw images into 3D reconstructed images. The bone volume/tissue volume (BV/TV), Bone surface/tissue volume (BS/TV), bone surface/bone volume (BS/BV) and bone mineral density (BMD) were evaluated and recorded, with n = 6 independent samples per group and time point.

2.9.3. Histological analysis

Bone samples (n = 3 samples for each group and time point) were decalcified using an EDTA solution (pH = 7.2; Servicebio) at room temperature with gentle shaking for up to 1 month. The paraffin-embedded sections were prepared as previously described (see section 2.5.3). Histological analyses, including HE and Masson trichrome stains, were conducted on paraffin-embedded sections, and the images were captured using a Pannoramic MIDI Slide scanner.

2.10. Statistical analysis

Each experiment was performed at least in triplicate and was repeated three times. Data analysis was conducted using GraphPad Prism 9.3.0 and SPSS 22.0 software. One-way analysis of variances (ANOVA) with Tukey's post hoc test was employed for comparisons among more than two groups. For the comparisons between two groups, a two-tailed Student's t-test analysis was performed. Quantitative data are presented as mean ± SD, with $^*p < 0.05$, $^{**}p < 0.01$ and $^{***}p < 0.001$ considered statistically significant.

3. Results

3.1. Characterization of NCM, HAp@NCM and PAH-ACP@NCM

Fig. 1a shows the graphical illustration of NCMP preparation inspired from MVs in biomineralization. To synthesize mineral precursors, PAH was introduced into a calcium phosphate oversaturated solution as nucleation inhibitor. The obtained PAH-ACP nanoclusters were subsequently incorporated into NCM, forming a well-mixed suspension to generate NCMP. NCM loaded with hydroxyapatite (HAp), referred to as NCMH, was also constructed. FE-SEM and EDS mapping were used to study the surface morphology and element distributions of the microspheres. The pure NCM exhibited a spherical shape with porous and distinct microporous structures woven from nanofibers with diameters of less than 50 nm (Fig. 1b and e). In contrast, most of the pores in NCMH were filled with crystalline materials (Fig. 1c and f), indicating the existence of HAp, as NCMH was subjected to heating at 80 °C for 48 h to accelerate crystal formation, transforming CaP into HAp. The micropores of NCMP were filled with mineral precursors that displayed no obvious crystallinity (Fig. 1d and g). AFM was utilized to investigate both the morphological characteristics and surface roughness of the microspheres (Fig. 1h). The NCM exhibited an average root mean square (RMS) roughness (Rq) of 269 nm ± 9.539 nm. The addition of HAp to the NCM (NCMH), did not notably modify the surface roughness, which is presumably attributable to the heterogeneous crystallization of HAp. In contrast, the loading of PAH-ACP to the NCM (NCMP) resulted in a significant reduction in surface roughness, decreasing to 142.7 nm ± 4.667 nm. This observation suggests that PAH-ACP can effectively smooth the NCM surface, likely due to its amorphous nature facilitating a more uniform coating. The size distribution of NCMP showed a narrow range from 60 to 110 μm, with a mean diameter of 86.77 μm (Fig. 1i).

To further investigate the chemical composition of the amorphous materials, EDS Mapping results showed that the distribution of Ca and P elements overlapped with the NCMP image, verifying the successful incorporation of PAH-ACP into NCMP (Fig. 1j). To ascertain whether the calcium phosphates loaded onto NCMP remained amorphous, FT-IR and XRD were performed to examine the crystalline phase of NCMP. The FT-IR and XRD spectra of NCM, NCMH and NCMP exhibited similar features, with absorption peaks corresponding to the C=O and N-H bonds, as well as characteristic diffraction peaks (020) and (110) associated with chitosan (Fig. 1k and l). Nevertheless, the FT-IR spectrum of NCMH revealed typical crystal absorption peaks of the P-O bond at 471, 567, 962 and 1035 cm^{-1}, while the XRD spectra showed distinctive peaks at 2θ values of 31.9° (211) indicatives of HAp. This observation indicated that the calcium phosphates in NCMH possess crystalline structures,

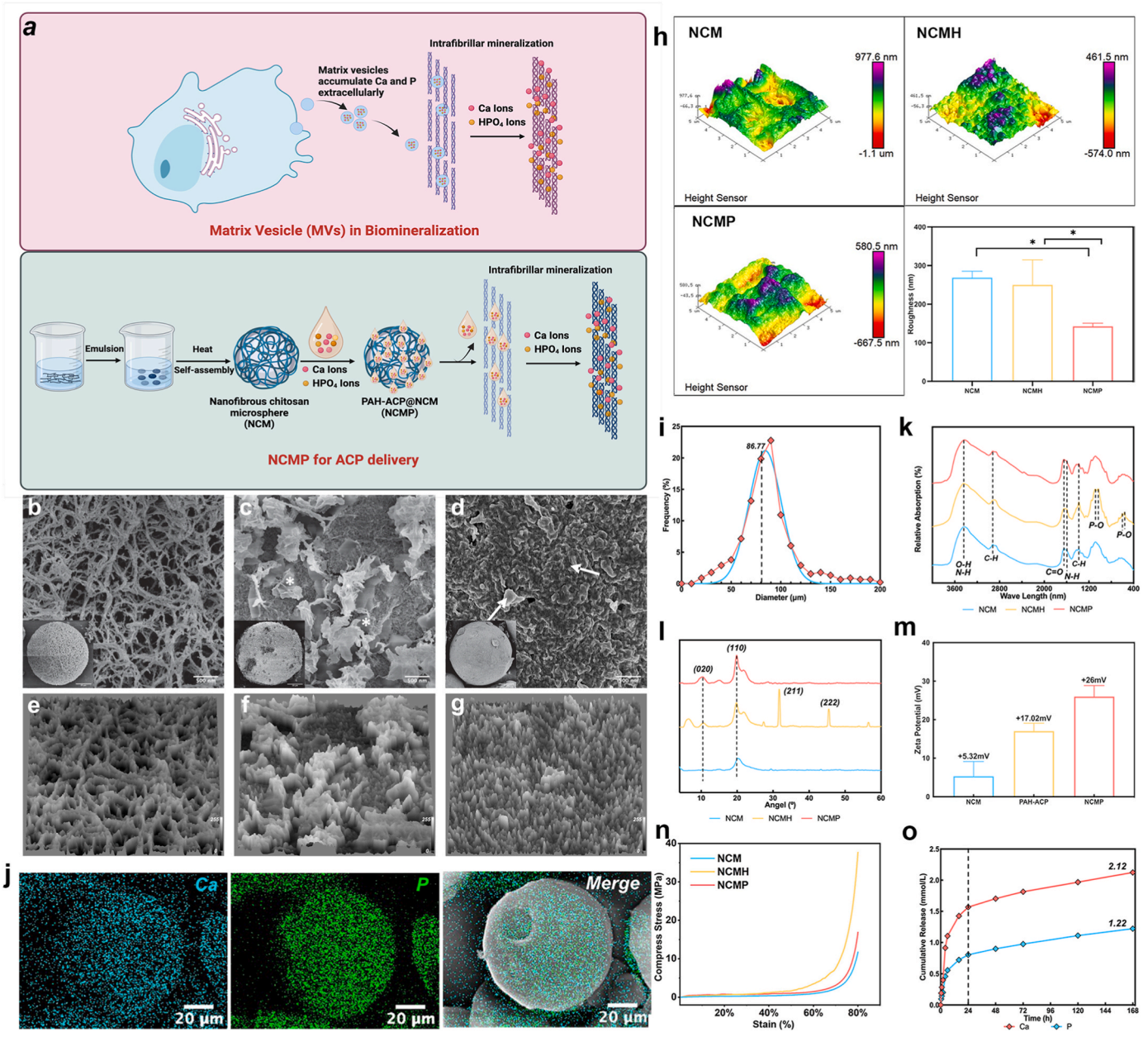

Fig. 1. Synthesis and characterization of NCMP. (a) Graphical illustration of NCMP developed via the incorporation of PAH-ACP with NCM inspired from MVs in biomineralization. SEM images (b–d) and 3D surface plots (e–g) of NCM (b, e), NCMH (c, f) and NCMP (d, g), with inserts on the left bottom corner showing the macro morphology. White asterisks indicate fibrous structures, while white arrows highlight the amorphous substances covering on the surface. (h) AFM images of surface topography and roughness of different groups. (i) Size distribution of NCMP, the red dots and line shows the frequency, while the blue curve serves as the fitted line. (j) Distribution of Ca and P on the surface of NCMP as analyzed by SEM-EDX. (k–l) FTIR (k) and XRD (l) spectra of NCM, NCMH and NCMP. (m) Zeta potential of NCM, NCMP and PAH-ACP. (n) Compressive stress analysis of NCM, NCMH and NCMP. (o) Cumulative release profiles of Ca and P ions from NCMP. (For interpretation of the references to color in this figure legend, the reader is referred to the Web version of this article.)

whereas those in NCMP remain amorphous. To further explore the mechanism underlying the successful incorporation of PAH-ACP, the zeta potentials of NCM, PAH-ACP and NCMP were assessed (Fig. 1m). The average zeta potential of NCM was +5.32 mV, while PAH-ACP showed a positive potential of +17.03 mV. After loading the microspheres with PAH-ACP, the overall zeta potential increased to +26.00 mV. The dramatic shift in zeta potential after loading PAH-ACP verified the successful incorporation of PAH-ACP into NCMP.

Mechanical performance under identical strain conditions were tested for each group (Fig. 1n). At a strain level of 80 %, the observed stress values establish a distinct hierarchy: NCM exhibits the lowest stress at 11.73 MPa, NCMP follows with 16.87 MPa, and NCMH shows the highest stress at 37.66 MPa. These variations can be attributed to the differential structural reinforcement imparted by the incorporated materials. The NCM, composed solely of chitosan, lacks additional strengthening agents, resulting in the lowest stress-bearing capacity. The inclusion of PAH-ACP in NCMP enhances mechanical properties due to effective interfacial interactions between chitosan and the amorphous calcium phosphate phase. As anticipated, the integration of apatite in NCMH offers superior mechanical reinforcement attributable to its higher stiffness and strength.

The cumulative release of calcium and phosphate ions from NCMP presented two distinct phases: the first phase involved a rapid release over the initial 24 h, followed by a second phase characterized by slow

and continuous release from day 1 to day 7 (Fig. 1o). The total concentrations of released calcium and phosphate ions were 2.12 and 1.22 mmol/L, respectively.

In summary, the mineralization precursor PAH-ACP was successfully incorporated into NCMP, maintaining its amorphous state, and demonstrating the ability to be released from NCMP when immersed within body fluid. Therefore, NCMP holds significant potential for the delivery of mineralization precursors, analogous to matrix vesicles (MVs).

3.2. Collagen intrafibrillar mineralization

The *in vitro* collagen intrafibrillar mineralization was evaluated using self-assembled collagen models. Numerous PAH-ACP clusters were released from the NCMP after 1 day and adhered to the surface of collagens (Fig. 2g). By 3 days, crystallinity began to emerge in the ACP clusters, with some infiltrating the collagen fibrils and resulting in partial mineralization (Fig. 2h). After 5 days, the electron densities throughout the collagen fibrils significantly increased, and the crystallinity of the nanocrystals became more apparent (Fig. 2i). SAED image revealed several arc-shaped diffraction patterns, indicating the existence of crystallinity within the collagen fibrils, with the diffraction pattern at the (002) plane indicating mineral deposition alongside these collagen fibrils. In contrast, the NCM and NCMH groups exhibited no evidence of mineralization even after 5 days (Fig. 2a–f), which was also corroborated by SAED results. Our experimental results demonstrated that collagen fibrils can achieve pronounced intrafibrillar mineralization within 5 days in the presence of NCMP. Altogether, NCMP can function similarly to MVs by allowing PAH-ACP released from NCMP to retain its amorphous state, thereby infiltrating and mineralizing collagen fibrils (Fig. 2j), highlighting its potential application in bone tissue regeneration.

3.3. Biocompatibility

To thoroughly assess the biosafety of NCMP, the CCK-8 test was conducted with different amount of NCMP. Cell colonization and proliferation were recorded and analyzed at specific time points (1, 3, 5 and 7 days) (Fig. 3a). The absorptions values at 450 nm for each group increased over time and showed no significant differences compared to the control group, suggesting the excellent biocompatibility of the NCMP scaffolds. Crystal violet staining showed that cells proliferated extensively after 5 days of culture compared to those after 1 day (Fig. 3b), with no significant differences observed between the NCMP and control group.

Hemolytic assessment was performed to verify the effect of NCMP on blood cells and the formation of blood clots (Fig. 3c and d). The ddH_2O group (Control+) presented as a bright red solution due to the release of hemoglobin from ruptured red cells. In contrast, the PBS group (Control-) remained colorless and transparent, showing that hemolysis was effectively avoid. The hemolysis rate for all NCMP groups (5, 10 and 20 mg/mL) was no greater than 5 %, suggesting that the NCMP scaffolds considered safe according to the ISO standard. Coomassie brilliant blue staining, which binds to microfilaments or tubulin, showed clear and well-stretched filamentous actin in all groups (Fig. 3e), suggesting a favorable niche for the cells.

The fluid absorption and degradation abilities of NCMP were measured through immersion in TBS or lysozyme solution (Fig. 3f). The absorption rate of NCMP after 12 h was 484.15 %, suggesting the excellent ability to absorb and concentrate nutrients, cytokines, and growth factors from body fluids. Subsequently, the NCMP presented significant weight loss due to lysozyme activities, with values of 79.75 % $\pm$ 0.51 % for 10 mg/mL and 55.14 % $\pm$ 0.19 % for 1 mg/mL, suggesting their excellent biodegradation properties. The *in vivo* biodegradation of NCMP was investigated by implanting the materials into subcutaneous tissues of Rats. After one day, inflammatory cells infiltrated around the NCMP materials, indicating a mild inflammatory response resulting from the surgical procedure and the implanted materials (Fig. 3g). After 4 weeks, the inflammatory response gradually subsided alongside the degradation of the NCMP. By 8 weeks, inflammatory cells were nearly absent at the surgical sites, and most of the microspheres had been absorbed, indicating excellent biodegradable properties.

3.4. Cell adhesion

To evaluate cell adhesion, hDPSCs were seeded onto NCMP microspheres to establish a 3D culture system. After culturing for 1 week, most cells attached and grew onto the NCMP scaffolds, transforming the loose microspheres into a macroscopic cell-NCMP complex measuring centimeters in size. A steel tweezer could even lift the 3D complex (Fig. 4a and b). The captured images demonstrated that the cells colonized the microspheres (Fig. 4c and d), with dark-purple cell nuclei clearly visible, confirming the presence of attached cells following crystal violet staining (Fig. 4e and f). SEM images (Fig. 4h) provided a more detailed view of the cells colonizing the scaffolds, showing that the filopodia extended and anchored to the matrix surface. After one day of culture, specific gene markers related to cell adhesion were assessed using qPCR, revealing that the transcribed mRNA levels in NCMP group were significantly higher compared to the control group, indicating a strong affinity between the cells and NCMP (Fig. 4g).

Meanwhile, the cytoskeleton and nucleus of hDPSCs were stained to assess cell adhesion and spreading (Fig. 4i). Most cells adhered tightly to the surface of the microspheres, in contrast to the control groups where cells spread randomly, indicating that cells are more likely to grow on the scaffolds. The relative intensity of filamentous actin (Fig. 4j and k) in NCMP group was significantly stronger compared to the control group. This study confirmed that the addition of PAH-ACP did not compromise the biocompatibility of the NCMP materials, which continue to serve as excellent scaffolds for cell migration, adhesion, and proliferation.

3.5. In vitro immunological regulation

In this study, mouse macrophages RAW 264.7 were co-cultured with different microspheres to examine the immunomodulatory effects *in vitro*. After co-culturing the RAW 264.7 cells with the microspheres for 1 and 2 days, qPCR was performed to assess the expression levels of macrophage polarization-related genes. Compared to the NCM and NCMH groups, the NCMP group showed a significant upregulation in the gene expression of M2 markers and anti-inflammatory cytokines (Fig. 4l), including CD-206, IL-10, and ARG-1. Conversely, there was a notable decrease in the expression of M1 markers and osteoclast-related factors, such as CD-11c, RANK, and MMP-9, in the NCMP groups (Fig. 4l). These findings suggest that NCMP promotes M2 polarization of macrophages, potentially reducing inflammatory response and fostering a pro-osteogenic microenvironment.

3.6. In vitro osteogenic differentiation

The ALP activity was investigated to evaluate the early stages of osteogenic differentiation. The ALP staining results showed that hDPSCs cultured with NCMP presented the most favorable area compared to all other groups after 1 and 2 weeks (Fig. 5a), which was further verified by relative quantitative results of ALP activities (Fig. 5c). To investigate the late stage of osteogenic differentiation, the mineral deposits and calcium

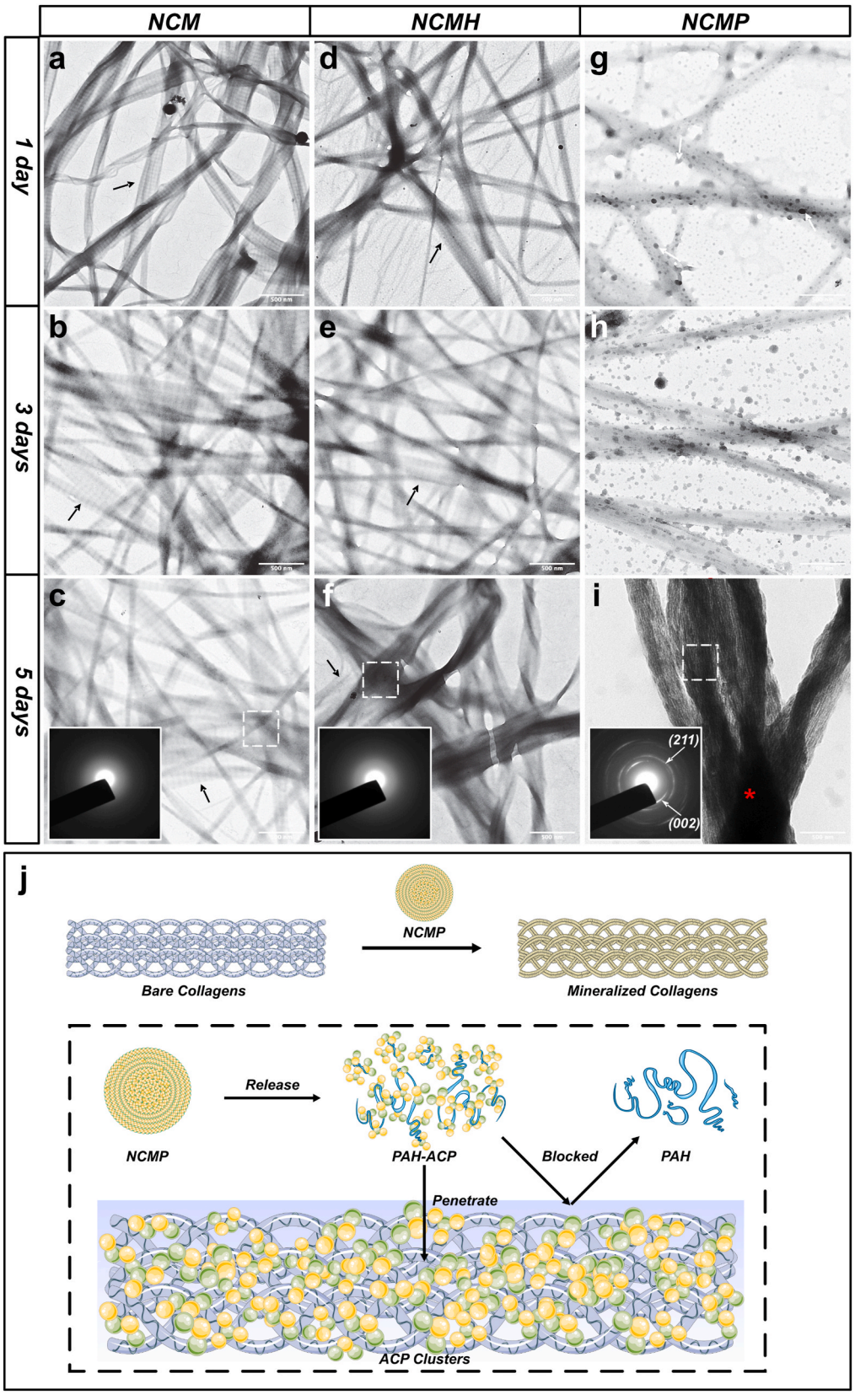

Fig. 2. *In vitro* collagen intrafibrillar mineralization of NCMP. (a–i) TEM images of single-layer collagen with NCM, NCMH and NCMP at 1 day, 3 days and 5 days, with inserts illustrating the SAED images of collagens after 5 days. Black arrows indicate non-mineralized collagens, white arrows indicate stabilized ACP clusters adhered to the collagen, and red asterisks indicate mineralized collagens. (j) Graphical illustration of the possible mechanism of NCMP in the collagen mineralization process. (For interpretation of the references to color in this figure legend, the reader is referred to the Web version of this article.)

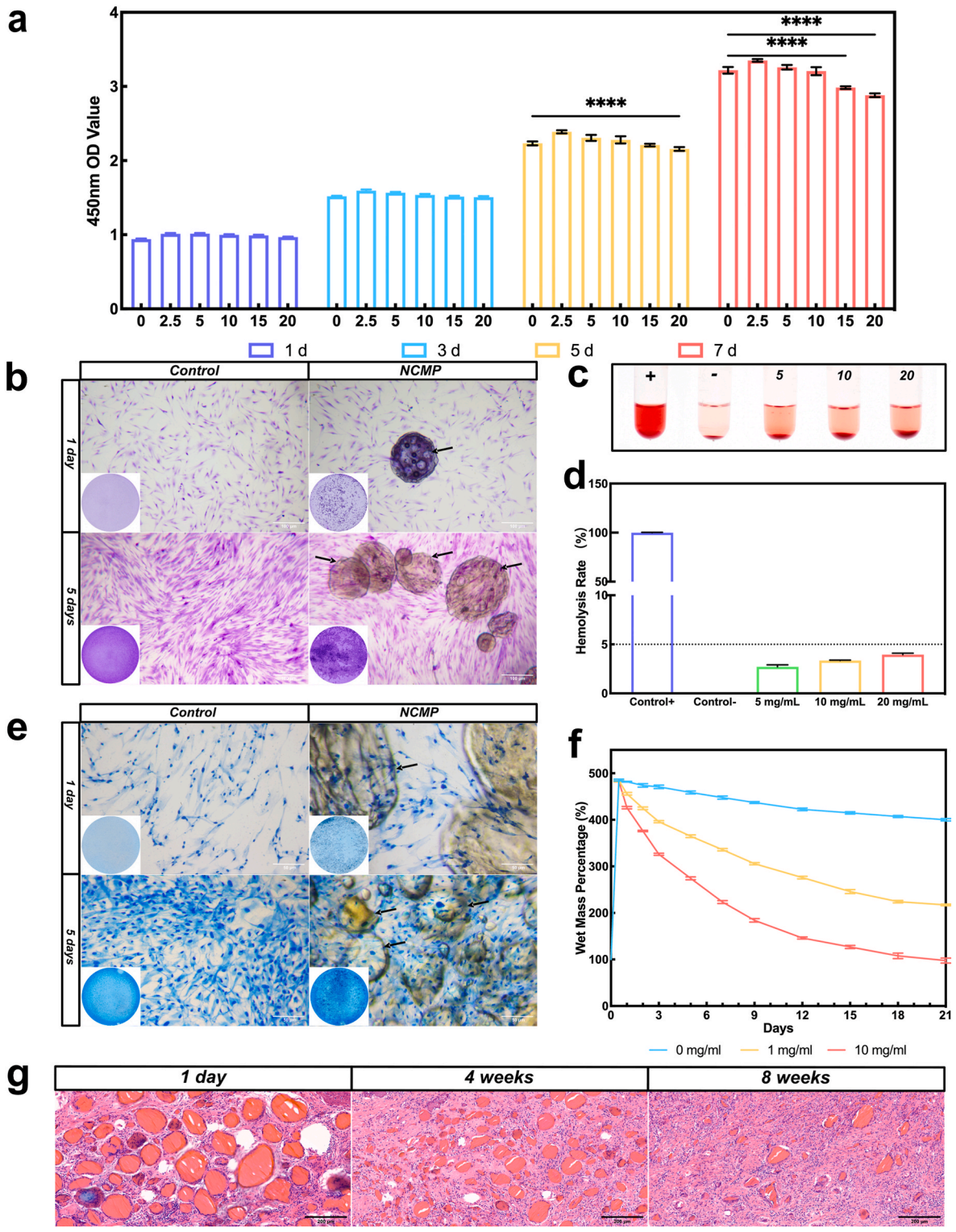

Fig. 3. Biocompatibility assessment of NCMP. (a) CCK-8 results of hDPSCs cultured with NCMP at different concentrations after 1, 3, 5 and 7 days. (b) Optical micrographs with crystal violet staining of hDPSCs, the inserts show the macro view, black arrows indicate NCMP materials. (c–d) Images of hemolysis (c) and the corresponding hemolysis rate (d) of NCMP. (e) Optical micrographs of hDPSCs with coomassie brilliant blue staining, the inserts show the macro view, black arrows indicate NCMP materials. (f) *In vitro* degradation of NCMP at varying lysozyme concentrations (0, 1, 10 mg/mL). (g) Optical micrographs of NCMP *in vivo* with HE staining following implantation for specific time intervals. (For interpretation of the references to color in this figure legend, the reader is referred to the Web version of this article.)

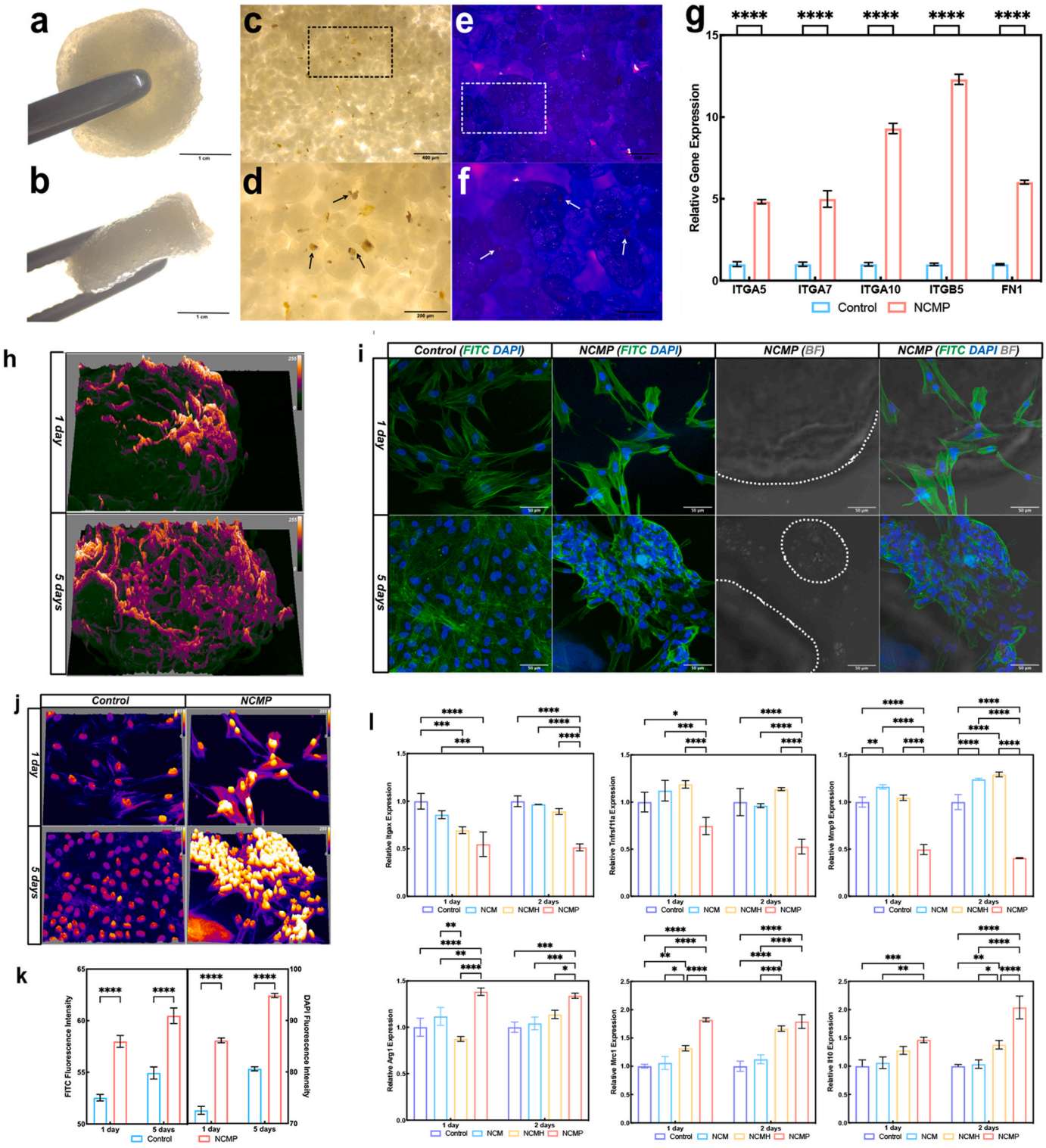

Fig. 4. Cell adhesion assessment and immunoregulatory effect of NCMP. (a–b) Macrographs of the cell-NCMP aggregates presented from the front view (a) and side view (b). (c–f) Optical micrographs of the cell-NCMP aggregates, shown in bright-field (c–d) and following crystal violet staining (e–f), with arrows indicating colonized hDPSC cells. (g) qPCR analysis of adhesion-related genes expression of hDPSCs after 24 h culture. (h) SEM images with 3D surface plots of cells colonized on NCMP after 1 day and 5 days, pseudo colors were applied to distinguish attached cells (purple) from microspheres (dark green). (i) CLSM images of cell adhesion after 1 and 5 days, with bright field indicating as BF and white dotted lines outlining the microspheres. (j) The 3D surface plots of (i) with pseudo colors. (k) Semi-qualification results of fluorescence intensity of (i). (l) *In vitro* assessment of macrophage polarization-related genes expression. qPCR analysis of genes expression of M1 markers and osteoclast-related factors in RAW 264.7s at 1 and 2 days: CD-11c (Itgax), RANK (Tnfrsf11a), MMP-9 (Mmp9); gene expression of M2 markers and anti-inflammatory cytokines in RAW 264.7 at 1 and 2 days: ARG-1 (Arg1), CD-206 (Mrc1), IL-10 (Il10). (For interpretation of the references to color in this figure legend, the reader is referred to the Web version of this article.)

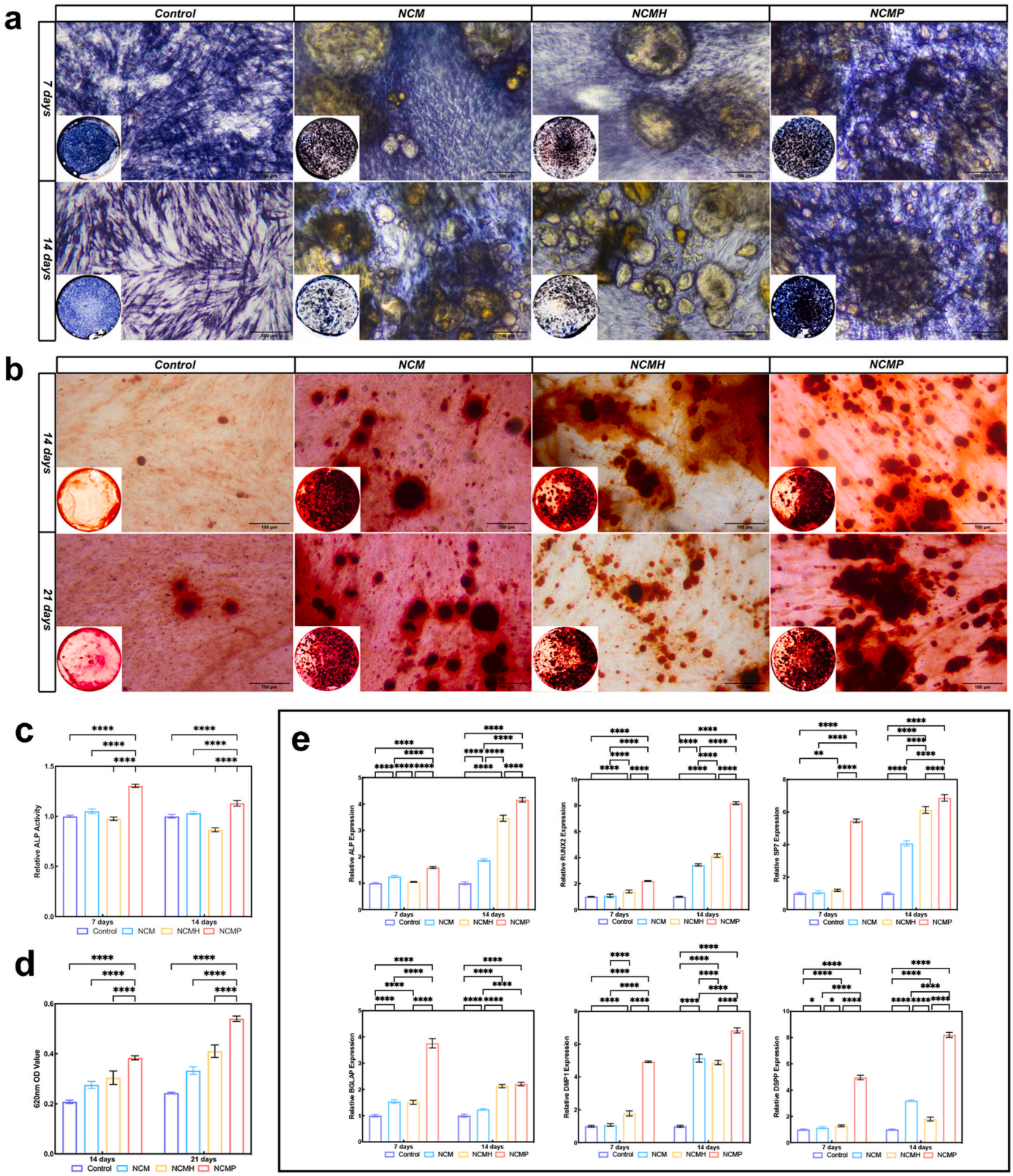

Fig. 5. *In vitro* osteogenic differentiation of NCMP. (a–b) Optical micrographs of hDPSCs with ALP staining (a) and Alizarin Red Staining (b) in Control, NCM, NCMH and NCMP groups, the inserts show the macro view. (c) Relative ALP activity of hDPSCs at 7, 14 days. (d) Semi-quantitative analysis of Alizarin Red staining of hDPSCs at 14, 21 days. (e) qPCR analysis of osteogenic-related genes expression of hDPSCs at 7, 14 days. n = 3 independent samples per group. (For interpretation of the references to color in this figure legend, the reader is referred to the Web version of this article.)

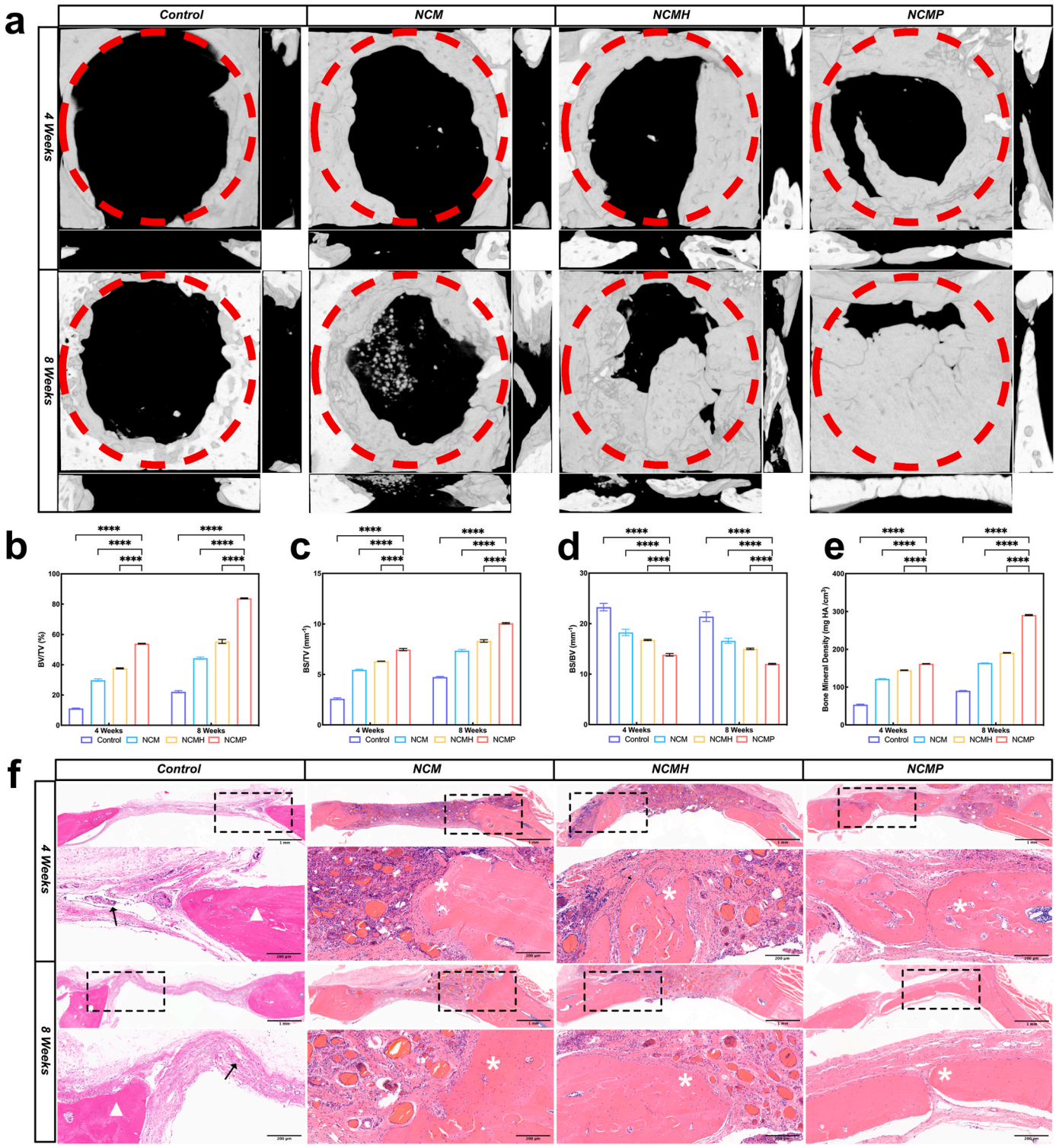

Fig. 6. *In vivo* assessment of NCMP in rat bone defect models. (a) 3D reconstruction images of bone samples at 4 and 8 weeks; Red dotted circle indicated the original critical-size (5 mm in diameters) bone defects. (b–e) Quantitative analysis of bone formation by BV/TV (b), BS/TV (c), BS/BV (d) and BMD (e). (f) Optical micrographs of representative bone samples with HE staining at 4 and 8 weeks, white triangles show the host bone, black arrows show the fibrous tissue, and white asterisks indicate the formation of new bone. (For interpretation of the references to color in this figure legend, the reader is referred to the Web version of this article.)

nodules formed among cells were investigated using ARS. The ARS staining results showed an obvious increase in mineral deposits in the NCMP groups after 2 and 3 weeks of induction (Fig. 5b), which was also supported by quantitative results of absorbance at 620 nm from ARS dyes bonded to mineral deposits (Fig. 5d). Additionally, the mRNA levels of osteogenic related genes in hDPSCs were significantly increased in NCMP group after 7 or 14 days of induction, suggesting a robust and long-lasting osteogenic induction (Fig. 5e). Overall, the results indicate that NCMP possesses excellent osteoinductive ability *in vitro*.

3.7. In vivo bone regeneration

Micro-CT and 3D reconstruction were conducted to analyze the bone formation and regeneration at specific time point. Eight weeks post-surgery, the 3D reconstruction results showed that significant bone defects persisted in the Control group (Fig. 6a). In contrast, new bone growth radiated from the edges toward the center of the defect areas in the NCM group after 8 weeks, which indicated that chitosan microspheres alone slightly promoted bone regeneration. The NCMP group exhibited obvious bone bridging and defect reunion, outperforming all other groups. Quantitative results regarding the newly formed bone at the surgical sites were assessed using the Micro-CT bundled software. After 8 weeks, the BV/TV (Fig. 6b) and BS/TV (Fig. 6c) in the defect areas indicated that the NCMP group had the highest amount of newly formed bone compared to all other groups. The BS/BV (Fig. 6d) in the NCMP group was the lowest among all groups, suggesting that the newly formed bone transitioned from granules to lamellar bone. The BMD analysis (Fig. 6e) indicated that the new bone formed with NCMP microspheres exhibited the highest bone density, underscoring the significant contribution of PAH-ACP released from NCMP to the mineral disposition and bone formation.

HE and Masson trichrome staining were conducted to evaluate the total amounts and structures of newly formed bones. After 4 and 8 weeks of implantation, HE staining (Fig. 6f) and Masson trichrome staining

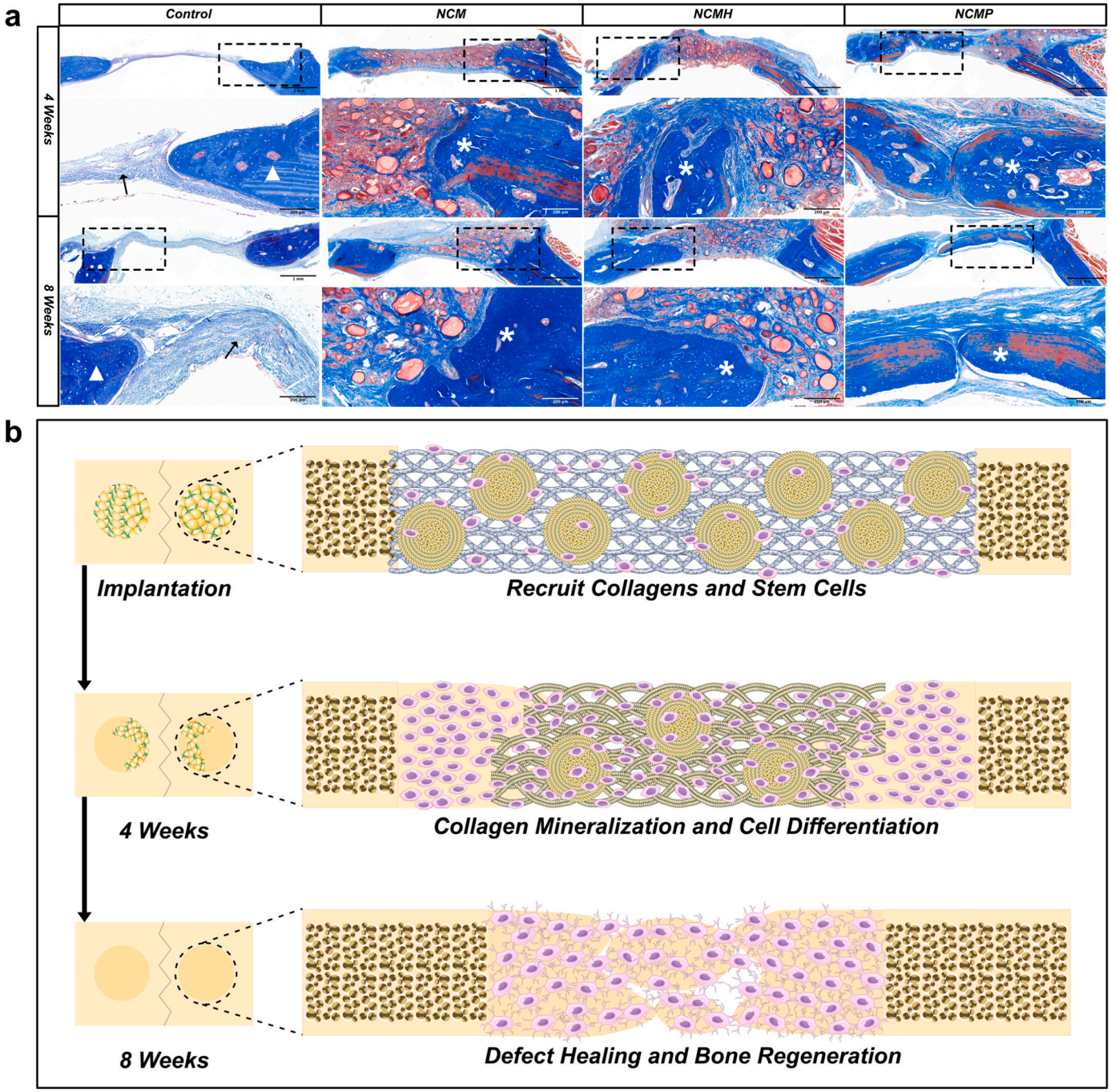

Fig. 7. *In vivo* assessment of NCMP in rat bone defect models. (a) Optical micrographs of representative bone samples with Masson Trichrome staining at 4 and 8 weeks, white triangles show the host bone, black arrows show the fibrous tissue, and white asterisks indicate the formation of new bone. (b) Graphical illustration of possible procedures of NCMP in the bone repair process.

images (Fig. 7a) showed that the bone defects in the control group remained empty, without obvious bone formation. The NCMP microspheres showed excellent properties for bone defect healing, presenting clear and continuous outlines of the context, with the total amount of newly formed bone significantly greater than in all other groups. Moreover, some of the newly formed bone in NCMP groups even showed marrow-like structures, indicating that they had developed fairly mature structures capable of supporting physical and biological functions.

4. Discussion

When initiating biomineralization *in vitro*, three main components need to be combined: collagen fibrils, minerals, and non-collagenous protein (NCP) mimics or analogs, such as PAA, PAsp, PAH and PAMAM [40]. Collagen fibrils have nucleation sites to bind with ACP [24,41] and guide the periodic deposition of hydroxyapatite within collagen fibrils along the long axis [42], which was referred to as intrafibrillar mineralization. In this study, we employed PAH as the nucleation inhibitor to fulfill intrafibrillar mineralization. The mechanisms of size exclusion [43] and the establishment of the Gibbs-Donnan equilibrium [25] provide insights into how the positively charged PAH-ACP aids collagen mineralization. In the presence of PAH, ACP remains the form of moldable nanoclusters in an amorphous state, smaller than 6 kDa, allowing them to infiltrate collagen fibrils. Due to its substantial molecular weight, PAH was blocked from influx into the intrafibrillar zone. The accumulation of PAH outside the collagen fibrils increases osmotic pressure, enhancing the driving force for ACP to penetrate the fibrils and restore the equilibrium between electrostatic interactions and osmotic pressure inside and outside collagen fibrils [25]. Therefore, PAH-stabilized ACP can be delivered into bone defect areas to initiate biomineralization serving as the inorganic phase, presenting a promising technique for bone tissue engineering strategies (Fig. 7b).

Polymeric nanofibers are excellent scaffolds as they can reconstruct and replicate the 3D microenvironment of ECM, thereby supporting cell infiltration and colonization both *in vitro* or *in vivo* [44]. Additionally, the large surface area provided by the fibrous structure is advantageous for the encapsulation of bioactive molecules, such as PAH-ACP [45,46]. In this study, nanofibrous chitosan microspheres (NCM) were successfully prepared from a chitosan alkaline/urea aqueous solution, as detailed in our previous study [37]. Featuring micropore/tunnel structures and primary amine functional groups, NCM holds enormous potential for modifying its bioactive and mechanical properties by incorporating inorganic minerals. Given that ACP loaded on NCMP remains amorphous, the mineralization precursors can be released from microspheres to progress intrafibrillar mineralization.

Besides intrafibrillar mineralization, PAH-ACP can directly regulate osteogenic differentiation. In this study, hDPSCs were used *in vitro* to evaluate the osteogenic efficiency of the MVs-like ACP carrying NCMP system. hDPSCs have been widely used in bone tissue engineering due to enormous differentiation potential into osteogenic cell lines [47], with gene expression profiles similar to BMSCs [48]. In the present study, NCMP continuously released PAH-ACP, which promoted ALP activity, upregulated the expression of osteogenic genes, and induced mineral deposition, in addition to facilitating collagen mineralization and matrix reconstruction. Extracellular calcium gradients serve as powerful chemical signals to recruit surrounding cells to defect regions [49], while phosphates ions regulate cell cycle pathways to enhance cell proliferation [50,51]. This performance surpassed that of HAp-loaded NCM (NCMH). HAp, a natural compound found in bones and teeth, mainly forms from ACP *in vivo* and is present in hard tissues during initial mineral deposition [52]. The poor degradation and resorption rate makes it challenging for osteoprogenitors to interact and utilize, thereby limiting bone neoformation efficiency [53]. Additionally, HAp crystallites are found to be phagocytized by resident cells, which subsequently induces pyroptosis [54]. Consequently, NCMP showed excellent osteoinductivity and proved to be suitable for optimal bone regeneration.

Biocompatibility is a crucial prerequisite in determining the application potential of a bone-grafting material. For a scaffold to be considered biocompatible, it must function effectively in the aimed environment without causing any local or systemic side effects [55]. Therefore, it is important to evaluate the potential impact of NCMP on cell behavior, interactions with blood cells, and biodegradability. Organs are 3D arrangements of cells that exhibit intricate interactions both among cells themselves and between cells and ECM, facilitating the free movement and exchange of nutrients and signals [56]. Therefore, biomimetic materials should prioritize enhancing cell colonization and adhesion to the scaffold matrix. In contrast to two-dimensional cell cultivation, the NCMP scaffold provide favorable environment for cells to adhere, spread, proliferate, and differentiate. Cell-matrix adhesions are transmembrane linkages that connect the ECM to the actin cytoskeleton, consisting of ECM proteins, integrin clusters, and submembrane adhesion protein aggregates [57]. Integrins, a prominent family of cell surface receptors, play a critical role in cell mobilization and colonization [58], and are likely the primary components activated by the NCMP scaffold to promote bone regeneration [59]. Blood compatibility is a crucial consideration for materials that come into direct contact with blood. Hemolysis rate is an important metric for assessing the impact of materials on red blood cells. For biomaterials in contact with blood, the hemolysis rate should be less than 5 % according to the ISO standard [60]. Materials with higher hemolysis rates can cause significant rupture of red blood cells, potentially leading to thrombosis and implant failure [61]. Here, the hemolysis rates of all NCM groups were lower than 5 %, suggesting good hemocompatibility. Controlled biodegradability is essential for creating space during tissue regeneration and remodeling; however, delayed degradation may hinder the penetration and growth of new tissue, thereby prolonging the regeneration process [62]. The enzyme lysozyme facilitates the degradation of chitosan by catalyzing the hydrolysis of the β-1,4-glycosidic bond between N-acetyl-glucosamine and glucosamine, with the degradation rate being proportional to the numbers of units in the chitosan molecule [63]. Compared to conventional bone grafts, the NCM exhibit excellent biodegradability, making them ideal for bone regeneration and eliminating the need for subsequent surgeries to remove the implant.

NCMP possesses excellent osteoinductive and immunomodulatory ability *in vitro*, which may promote M2 polarization of macrophages, potentially reducing inflammatory response, and foster a pro-osteogenic microenvironment. The *in vivo* osteoinductive properties of the NCMP for optimal regeneration was further investigated with rat bone defect models. The defects, 5 mm in diameter, were created in the calvarial bone of SD rats and, which typically could not heal spontaneously throughout the animals' lifespan [64]. Following the creation of these bone defects, all models were randomly divided to four groups (Control, NCM, NCMH and NCMP), and the corresponding microspheres were implanted at the defect area. The sustainable release of PAH-ACP and nanofibrous structures of the NCMP promote cell colonization, adhesion, proliferation, and differentiation, facilitating collagen formation in the defect area. Simultaneously, the stabilized ACP precursor stored from NCMP carrier infiltrate collagen to achieve collagen mineralization. The NCMP scaffold also enhances immunoregulation by promoting M2 polarization, swiftly resolving inflammation and fostering a pro-healing environment. Altogether, these findings confirm that NCMP successfully integrate biological functions of PAH-ACP and the ECM-mimicking nanofibrous structure, significantly contributing to effective bone repair and regeneration.

5. Conclusion

The present study successfully synthesized a novel bio-delivery system (NCMP) by incorporating polymer-induced mineralization precursors (PAH-ACP) into nanofibrous chitosan microspheres (NCM). The

sustainable release of PAH-ACP allows for infiltration into collagen fibrils, facilitating intrafibrillar mineralization. The NCMP promotes cell adhesion and proliferation, thereby benefiting osteogenic differentiation and enhancing bone regeneration. This work demonstrates that the NCMP effectively functions as both a delivery vehicle for mineralization precursors and an ECM-mimicking bio-block, achieving a synergistic effect between cell-free and cell-dependent biomineralization, thereby obtaining optimal application in bone repair and regeneration.

CRediT authorship contribution statement

Haolin Bian: Writing – review & editing, Writing – original draft, Methodology, Formal analysis, Data curation, Conceptualization. **Fangfang Song:** Writing – review & editing, Writing – original draft, Validation, Data curation. **Shilei Wang:** Writing – original draft, Methodology, Data curation. **Wei Sun:** Methodology, Data curation. **Bo Hu:** Methodology, Data curation. **Xichao Liang:** Methodology, Data curation. **Hongye Yang:** Writing – review & editing, Supervision, Resources, Project administration, Investigation, Funding acquisition, Data curation, Conceptualization. **Cui Huang:** Writing – review & editing, Validation, Supervision, Project administration, Investigation, Funding acquisition.

Declaration of competing interest

The authors declare that they have no known competing financial interests or personal relationships that could have appeared to influence the work reported in this paper.

Acknowledgements

This work was supported by the National Natural Science Foundation of China (82371004,82271010), Hubei Provincial Natural Science Foundation of China (2024AFB738), and the Fundamental Research Funds for the Central Universities (2042024YXB020).

Data availability

Data will be made available on request.

References

[1] L. Dejob, B. Toury, S. Tadier, L. Gremillard, C. Gaillard, V. Salles, Electrospinning of in situ synthesized silica-based and calcium phosphate bioceramics for applications in bone tissue engineering: a review, Acta Biomater. 123 (2021) 123–153.
[2] E.H. Schemitsch, Size matters: defining critical in bone defect size, J. Orthop. Trauma 31 (Suppl 5) (2017) S20–S22.
[3] Z. Peng, T. Zhao, Y. Zhou, S. Li, J. Li, R.M. Leblanc, Bone tissue engineering via carbon-based nanomaterials, Adv Healthc Mater 9 (5) (2020) e1901495.
[4] W. Wang, K.W.K. Yeung, Bone grafts and biomaterials substitutes for bone defect repair: a review, Bioact. Mater. 2 (4) (2017) 224–247.
[5] S.L. Wu, X.M. Liu, K.W.K. Yeung, C.S. Liu, X.J. Yang, Biomimetic porous scaffolds for bone tissue engineering, Mater. Sci. Eng. R Rep. 80 (2014) 1–36.
[6] A. Khademhosseini, R. Langer, A decade of progress in tissue engineering, Nat. Protoc. 11 (10) (2016) 1775–1781.
[7] M. Filippi, G. Born, M. Chaaban, A. Scherberich, Natural polymeric scaffolds in bone regeneration, Front. Bioeng. Biotechnol. 8 (2020) 474.
[8] D. de Melo Pereira, P. Habibovic, Biomineralization-inspired material design for bone regeneration, Adv Healthc Mater 7 (22) (2018) e1800700.
[9] J. Zhang, J. Deng, Y. He, J. Wu, M.F. Simoes, B. Liu, Y. Li, S. Zhang, A. Antunes, A review of biomineralization in healing concrete: mechanism, biodiversity, and application, Sci. Total Environ. 917 (2024) 170445.
[10] S. Tang, Z. Dong, X. Ke, J. Luo, J. Li, Advances in biomineralization-inspired materials for hard tissue repair, Int. J. Oral Sci. 13 (1) (2021) 42.
[11] T. Hasegawa, Ultrastructure and biological function of matrix vesicles in bone mineralization, Histochem. Cell Biol. 149 (4) (2018) 289–304.
[12] M.S. Yan Wei, Jinglun Zhang, Xiaoxin Zhang, Kailun Shen, Rui Wang, Richard J. Miron, Yin Xiao, Yufeng Zhang, Autologous versatile vesicles-incorporated biomimetic extracellular matrix induces biomineralization, Adv. Funct. Mater. 30 (21) (2020) 2000015.
[13] M. Bottini, S. Mebarek, K.L. Anderson, A. Strzelecka-Kiliszek, L. Bozycki, A.M. S. Simao, M. Bolean, P. Ciancaglini, J.B. Pikula, S. Pikula, D. Magne, N. Volkmann, D. Hanein, J.L. Millan, R. Buchet, Matrix vesicles from chondrocytes and osteoblasts: their biogenesis, properties, functions and biomimetic models, Biochim. Biophys. Acta Gen. Subj. 1862 (3) (2018) 532–546.
[14] T. Iwayama, P. Bhongsatiern, M. Takedachi, S. Murakami, Matrix vesicle-mediated mineralization and potential applications, J. Dent. Res. 101 (13) (2022) 1554–1562.
[15] R.E. Wuthier, G.F. Lipscomb, Matrix vesicles: structure, composition, formation and function in calcification, Front Biosci (Landmark Ed) 16 (8) (2011) 2812–2902.
[16] L. Cui, D.A. Houston, C. Farquharson, V.E. MacRae, Characterisation of matrix vesicles in skeletal and soft tissue mineralisation, Bone 87 (2016) 147–158.
[17] E.E. Golub, Role of matrix vesicles in biomineralization, Biochim. Biophys. Acta 1790 (12) (2009) 1592–1598.
[18] J. Yan, M. Shen, B. Sui, W. Lu, X. Han, Q. Wan, Y. Liu, J. Kang, W. Qin, Z. Zhang, D. Chen, Y. Cao, S. Ying, F.R. Tay, L.N. Niu, K. Jiao, Autophagic LC3(+) calcified extracellular vesicles initiate cartilage calcification in osteoarthritis, Sci. Adv. 8 (19) (2022) eabn1556.
[19] Y. Wang, X. Hu, L. Zhang, C. Zhu, J. Wang, Y. Li, Y. Wang, C. Wang, Y. Zhang, Q. Yuan, Bioinspired extracellular vesicles embedded with black phosphorus for molecular recognition-guided biomineralization, Nat. Commun. 10 (1) (2019) 2829.
[20] T. Sreenath, T. Thyagarajan, B. Hall, G. Longenecker, R. D'Souza, S. Hong, J. T. Wright, M. MacDougall, J. Sauk, A.B. Kulkarni, Dentin sialophosphoprotein knockout mouse teeth display widened predentin zone and develop defective dentin mineralization similar to human dentinogenesis imperfecta type III, J. Biol. Chem. 278 (27) (2003) 24874–24880.
[21] S. Ravindran, A. George, Multifunctional ECM proteins in bone and teeth, Exp. Cell Res. 325 (2) (2014) 148–154.
[22] J. Mahamid, B. Aichmayer, E. Shimoni, R. Ziblat, C. Li, S. Siegel, O. Paris, P. Fratzl, S. Weiner, L. Addadi, Mapping amorphous calcium phosphate transformation into crystalline mineral from the cell to the bone in zebrafish fin rays, Proc Natl Acad Sci U S A 107 (14) (2010) 6316–6321.
[23] S. Weiner, H.D. Wagner, The material bone: structure mechanical function relations, Annu. Rev. Mater. Sci. 28 (1998) 271–298.
[24] F. Nudelman, K. Pieterse, A. George, P.H. Bomans, H. Friedrich, L.J. Brylka, P. A. Hilbers, G. de With, N.A. Sommerdijk, The role of collagen in bone apatite formation in the presence of hydroxyapatite nucleation inhibitors, Nat. Mater. 9 (12) (2010) 1004–1009.
[25] L.N. Niu, S.E. Jee, K. Jiao, L. Tonggu, M. Li, L. Wang, Y.D. Yang, J.H. Bian, L. Breschi, S.S. Jang, J.H. Chen, D.H. Pashley, F.R. Tay, Collagen intrafibrillar mineralization as a result of the balance between osmotic equilibrium and electroneutrality, Nat. Mater. 16 (3) (2017) 370–378.
[26] R.A. Perez, S.J. Seo, J.E. Won, E.J. Lee, J.H. Jang, J.C. Knowles, H.W. Kim, Therapeutically relevant aspects in bone repair and regeneration, Mater. Today 18 (10) (2015) 573–589.
[27] F.N. Syed-Picard, T. Jayaraman, R.S. Lam, E. Beniash, C. Sfeir, Osteoinductivity of calcium phosphate mediated by connexin 43, Biomaterials 34 (15) (2013) 3763–3774.
[28] A. Lotsari, A.K. Rajasekharan, M. Halvarsson, M. Andersson, Transformation of amorphous calcium phosphate to bone-like apatite, Nat. Commun. 9 (1) (2018) 4170.
[29] C. Combes, C. Rey, Amorphous calcium phosphates: synthesis, properties and uses in biomaterials, Acta Biomater. 6 (9) (2010) 3362–3378.
[30] M.J. Olszta, X. Cheng, S.S. Jee, R. Kumar, Y.-Y. Kim, M.J. Kaufman, E.P. Douglas, L. B. Gower, Bone structure and formation: a new perspective, Mater. Sci. Eng. R Rep. 58 (3) (2007) 77–116.
[31] Y. Liu, Y.K. Kim, L. Dai, N. Li, S.O. Khan, D.H. Pashley, F.R. Tay, Hierarchical and non-hierarchical mineralisation of collagen, Biomaterials 32 (5) (2011) 1291–1300.
[32] B. Ye, X. Luo, Z. Li, C. Zhuang, L. Li, L. Lu, S. Ding, J. Tian, C. Zhou, Rapid biomimetic mineralization of collagen fibrils and combining with human umbilical cord mesenchymal stem cells for bone defects healing, Mater. Sci. Eng. C 68 (2016) 43–51.
[33] H.Y. Yang, L.N. Niu, J.L. Sun, X.Q. Huang, D.D. Pei, C. Huang, F.R. Tay, Biodegradable mesoporous delivery system for biomineralization precursors, Int J Nanomedicine 12 (2017) 839–854.
[34] S. Husain, K.H. Al-Samadani, S. Najeeb, M.S. Zafar, Z. Khurshid, S. Zohaib, S. B. Qasim, Chitosan biomaterials for current and potential dental applications, Materials 10 (6) (2017).
[35] C.H. Kim, S.J. Park, D.H. Yang, H.J. Chun, Chitosan for tissue engineering, Adv. Exp. Med. Biol. 1077 (2018) 475–485.
[36] D. Vukajlovic, J. Parker, O. Bretcanu, K. Novakovic, Chitosan based polymer/bioglass composites for tissue engineering applications, Mater Sci Eng C Mater Biol Appl 96 (2019) 955–967.
[37] H. Yang, S. Wang, H. Bian, X. Xing, J. Yu, X. Wu, L. Zhang, X. Liang, A. Lu, C. Huang, Extracellular matrix-mimicking nanofibrous chitosan microspheres as cell micro-ark for tissue engineering, Carbohydr. Polym. 292 (2022) 119693.
[38] H.D. Kim, S. Amirthalingam, S.L. Kim, S.S. Lee, J. Rangasamy, N.S. Hwang, Biomimetic materials and fabrication approaches for bone tissue engineering, Adv Healthc Mater 6 (23) (2017).
[39] L. Chen, X. Wang, S. Tian, L. Zhou, L. Wang, X. Liu, Z. Yang, G. Fu, X. Liu, C. Ding, D. Zou, Integrin-linked kinase control dental pulp stem cell senescence via the mTOR signaling pathway, Stem Cell. 42 (10) (2024) 861–873.
[40] B.M. Oosterlaken, M.P. Vena, G. de With, In vitro mineralization of collagen, Adv Mater 33 (16) (2021) e2004418.

[41] H.P. Schwarcz, D.M. Binkley, L. Luo, K. Grandfield, A search for apatite crystals in the gap zone of collagen fibrils in bone using dark-field illumination, Bone 135 (2020) 115304.
[42] D.R. Katti, S.M. Pradhan, K.S. Katti, Directional dependence of hydroxyapatite-collagen interactions on mechanics of collagen, J. Biomech. 43 (9) (2010) 1723–1730.
[43] P.A. Price, D. Toroian, J.E. Lim, Mineralization by inhibitor exclusion: the calcification of collagen with fetuin, J. Biol. Chem. 284 (25) (2009) 17092–17101.
[44] D.W. Hutmacher, J.T. Schantz, C.X. Lam, K.C. Tan, T.C. Lim, State of the art and future directions of scaffold-based bone engineering from a biomaterials perspective, J Tissue Eng Regen Med 1 (4) (2007) 245–260.
[45] S. Agarwal, J.H. Wendorff, A. Greiner, Progress in the field of electrospinning for tissue engineering applications, Adv Mater 21 (32–33) (2009) 3343–3351.
[46] A. Malek-Khatabi, H.A. Javar, E. Dashtimoghadam, S. Ansari, M.M. Hasani-Sadrabadi, A. Moshaverinia, In situ bone tissue engineering using gene delivery nanocomplexes, Acta Biomater. 108 (2020) 326–336.
[47] A. Graziano, R. d'Aquino, G. Laino, G. Papaccio, Dental pulp stem cells: a promising tool for bone regeneration, Stem Cell Rev. 4 (1) (2008) 21–26.
[48] S. Gronthos, M. Mankani, J. Brahim, P.G. Robey, S. Shi, Postnatal human dental pulp stem cells (DPSCs) in vitro and in vivo, Proc Natl Acad Sci U S A 97 (25) (2000) 13625–13630.
[49] G.E. Breitwieser, Extracellular calcium as an integrator of tissue function, Int. J. Biochem. Cell Biol. 40 (8) (2008) 1467–1480.
[50] K.A. Conrads, M. Yi, K.A. Simpson, D.A. Lucas, C.E. Camalier, L.R. Yu, T. D. Veenstra, R.M. Stephens, T.P. Conrads, G.R. Beck Jr., A combined proteome and microarray investigation of inorganic phosphate-induced pre-osteoblast cells, Mol. Cell. Proteomics 4 (9) (2005) 1284–1296.
[51] M. Julien, S. Khoshniat, A. Lacreusette, M. Gatius, A. Bozec, E.F. Wagner, Y. Wittrant, M. Masson, P. Weiss, L. Beck, D. Magne, J. Guicheux, Phosphate-dependent regulation of MGP in osteoblasts: role of ERK1/2 and Fra-1, J. Bone Miner. Res. 24 (11) (2009) 1856–1868.
[52] J. Mahamid, A. Sharir, L. Addadi, S. Weiner, Amorphous calcium phosphate is a major component of the forming fin bones of zebrafish: indications for an amorphous precursor phase, Proc. Natl. Acad. Sci. USA 105 (35) (2008) 12748–12753.
[53] A.S. AlGhamdi, O. Shibly, S.G. Ciancio, Osseous grafting part II: xenografts and alloplasts for periodontal regeneration–a literature review, J. Int. Acad. Periodontol. 12 (2) (2010) 39–44.
[54] T. Ye, C. Wang, J. Yan, Z. Qin, W. Qin, Y. Ma, Q. Wan, W. Lu, M. Zhang, F.R. Tay, K. Jiao, L. Niu, Lysosomal destabilization: a missing link between pathological calcification and osteoarthritis, Bioact. Mater. 34 (2024) 37–50.
[55] C. Xie, J. Ye, R. Liang, X. Yao, X. Wu, Y. Koh, W. Wei, X. Zhang, H. Ouyang, Advanced strategies of biomimetic tissue-engineered grafts for bone regeneration, Adv Healthc Mater 10 (14) (2021) e2100408.
[56] D. Antoni, H. Burckel, E. Josset, G. Noel, Three-dimensional cell culture: a breakthrough in vivo, Int. J. Mol. Sci. 16 (3) (2015) 5517–5527.
[57] E. Zamir, B. Geiger, Components of cell-matrix adhesions, J. Cell Sci. 114 (Pt 20) (2001) 3577–3579.
[58] S. Gronthos, P.J. Simmons, S.E. Graves, P.G. Robey, Integrin-mediated interactions between human bone marrow stromal precursor cells and the extracellular matrix, Bone 28 (2) (2001) 174–181.
[59] H.S. Kim, J.H. Lee, N. Mandakhbayar, G.Z. Jin, S.J. Kim, J.Y. Yoon, S.B. Jo, J. H. Park, R.K. Singh, J.H. Jang, U.S. Shin, J.C. Knowles, H.W. Kim, Therapeutic tissue regenerative nanohybrids self-assembled from bioactive inorganic core/chitosan shell nanounits, Biomaterials 274 (2021) 120857.
[60] C. Liu, H. Luo, M. Wan, L. Hou, X. Wang, Y. Shi, Strategy on biological evaluation for biodegradable/absorbable materials and medical devices, Bio Med. Mater. Eng. 29 (3) (2018) 269–278.
[61] M. Yang, Y. Zhang, F. Mou, C. Cao, L. Yu, Z. Li, J. Guan, Swarming magnetic nanorobots bio-interfaced by heparinoid-polymer brushes for in vivo safe synergistic thrombolysis, Sci. Adv. 9 (48) (2023) eadk7251.
[62] L. Crawford, M. Wyatt, J. Bryers, B. Ratner, Biocompatibility evolves: phenomenology to toxicology to regeneration, Adv Healthc Mater 10 (11) (2021) e2002153.
[63] K. Tomihata, Y. Ikada, In vitro and in vivo degradation of films of chitin and its deacetylated derivatives, Biomaterials 18 (7) (1997) 567–575.
[64] X. Wang, S. Xu, S. Zhou, W. Xu, M. Leary, P. Choong, M. Qian, M. Brandt, Y.M. Xie, Topological design and additive manufacturing of porous metals for bone scaffolds and orthopaedic implants: a review, Biomaterials 83 (2016) 127–141.